Spatiotemporal control of PopZ localization through cell cycle–coupled multimerization

Géraldine Laloux[1,2] and Christine Jacobs-Wagner[1,2,3]

[1]Department of Molecular, Cellular and Developmental Biology, [2]Howard Hughes Medical Institute, and [3]Department of Microbial Pathogenesis, Yale School of Medicine, Yale University, New Haven, CT 06511

Bacterial cell poles constitute defined subcellular domains where numerous proteins localize, often at specific times, to affect various physiological processes. How pole recognition occurs and what governs the timing of protein localization are often unknown. In this paper, we investigate the mechanisms governing the localization of PopZ, a chromosome-anchoring protein whose unipolar to bipolar localization pattern is critical for cell cycle progression in *Caulobacter crescentus*. We provide evidence that polar localization of PopZ relied on its self-assembly into a higher-order structure (matrix) and that the unipolar to bipolar transition was coupled to the asymmetric distribution of ParA during the translocation of the origin-proximal ParB–*parS* partition complex. Collectively, our data suggest a model in which a local increase of ParA concentration promotes the assembly of a PopZ matrix precisely when and where this matrix is needed. Such coupling of protein assembly with a cell cycle–associated molecular asymmetry may represent a principle of cellular organization for controlling protein localization in both time and space.

Introduction

Despite their relative small size and the lack of membrane-bounded organelles within their cytoplasm, bacterial cells display a remarkable level of spatial organization at the molecular level. In particular, the cell poles constitute a distinct subcellular environment in which a growing number of proteins have been found to localize (Rudner and Losick, 2010; Bowman et al., 2011). The resulting functional confinement is crucial for a broad variety of processes, including motility, chemotaxis, pathogenesis, cellular differentiation, and cell cycle progression. In many cases, a protein localizes at the cell pole through an interaction with an anchoring protein or complex that was already present at the pole, which raises the critical question of how the initial pole recognition is achieved. Geometric cues inherent to the cell poles, such as the degree of membrane curvature, can be "sensed" by some proteins (Lenarcic et al., 2009; Ramamurthi and Losick, 2009; Ramamurthi et al., 2009), but other self-organizing mechanisms likely exist to promote pole accumulation (Rudner and Losick, 2010). Another equally important and perhaps even less understood question regards the temporal dynamics of protein localization. Often, the protein localization pattern changes in time (for example, at a particular stage during the cell cycle). How this temporal regulation occurs remains largely elusive.

To examine these questions, we focused on the multimeric polar scaffold PopZ, whose dynamic localization pattern plays a crucial role during the cell cycle of *Caulobacter crescentus* (Fig. 1). In "swarmer" (G1 phase) cells, PopZ localizes at the old pole, where it forms a matrix that tethers the origin-proximal *parS* DNA sequence (and hence the chromosome) through a specific interaction with the *parS*-binding protein ParB (Bowman et al., 2008; Ebersbach et al., 2008). Initiation of DNA replication, which occurs only once per cell cycle, is quickly followed by the duplication of the *parS* sequences, resulting in two ParB–*parS* partition complexes (Mohl and Gober, 1997). Although one complex remains at the old pole, the other rapidly segregates toward the new pole, powered by the retraction of the DNA-bound ParA structure (Ptacin et al., 2010; Schofield et al., 2010; Shebelut et al., 2010). Around the same time, the localization pattern of PopZ becomes bipolar as a result of a new accumulation at the new pole, where PopZ captures the migrating ParB–*parS* complex (Bowman et al., 2008; Ebersbach et al., 2008). This unipolar to bipolar change in PopZ localization is a

Correspondence to Christine Jacobs-Wagner: christine.jacobs-wagner@yale.edu.

Abbreviations used in this paper: DIC, differential interference contrast; LB, Luria Bertani; LRI, low refractive index; TC, tetracysteine.

The Rockefeller University Press $30.00
J. Cell Biol. Vol. 201 No. 6 827–841
www.jcb.org/cgi/doi/10.1083/jcb.201303036

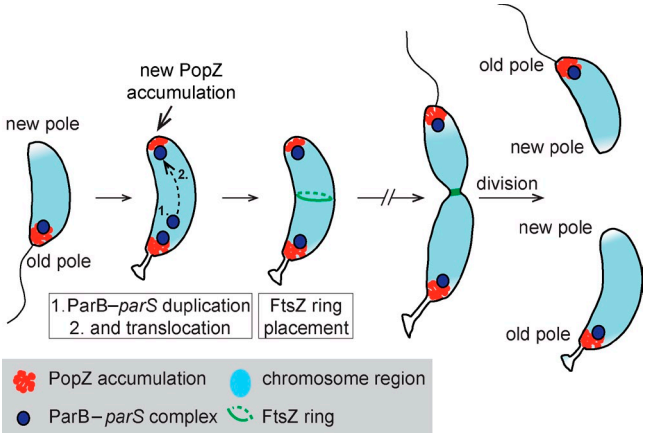

Figure 1. **Schematics of PopZ localization pattern during *C. crescentus* cell cycle.** See Introduction for details.

critical step for coordinating the initiation of chromosome segregation with the formation of the cytokinetic FtsZ ring. This is because the PopZ-dependent anchoring of the ParB–*parS* complexes at opposite poles stabilizes bipolar gradients of the FtsZ ring inhibitor MipZ, thereby promoting FtsZ ring assembly near the midcell where the MipZ inhibitory activity is the lowest (Thanbichler and Shapiro, 2006; Kiekebusch et al., 2012). Indeed, in Δ*popZ* cells, ParB–*parS* complexes, from which emanate the MipZ gradients, remain unanchored and thereby display considerable motion that affects the timing and location of FtsZ ring assembly (Ebersbach et al., 2008), leading to cell division defects (Bowman et al., 2008; Ebersbach et al., 2008). The dynamic localization pattern of PopZ is also important for other cell cycle–related events, as PopZ is essential for the polar localization of multiple cell cycle regulator proteins (Ebersbach et al., 2008; Bowman et al., 2010).

How PopZ accumulates at the poles and how it reproduces its dynamic localization pattern at every cell cycle remains poorly understood and is the subject of debates (Bowman et al., 2008, 2010; Ebersbach et al., 2008; Curtis and Brun, 2010; Rudner and Losick, 2010). In this work, we address both spatial and temporal aspects of PopZ localization. Our results support a simple model in which the ParA-dependent DNA segregation machinery controls the otherwise stochastic multimerization of PopZ spatially and temporally, such that a PopZ-anchoring matrix assembles at the right pole and at the right time during the cell cycle.

Results

Multimerization is required for polar localization

PopZ is known to self-assemble into oligomers that further assemble into a matrix (Bowman et al., 2008, 2010; Ebersbach et al., 2008). However, the importance of this assembly process in protein localization is unknown. To examine this question, we first sought to identify the regions within PopZ that are required for localization, oligomerization, and matrix formation inside cells. Because PopZ does not contain any domain of known function, we considered both the secondary structure prediction and the sequence conservation to delineate truncation boundaries. A multiple-sequence alignment of 100 PopZ orthologues highlighted the conservation of the N-terminal and C-terminal regions, which are predicted to form α helices (Fig. 2 A). We defined three main domains over the 177–amino acid sequence of PopZ (Fig. 2, A and B): (1) a conserved N-terminal domain composed mainly of an α helix (H1), (2) a central domain poorly conserved in sequence and size but characterized by a high content of proline residues, and (3) a conserved C-terminal domain, which includes three predicted α helices (H2 and the adjacent H3 and H4). We generated seven variants lacking various parts of the protein (Fig. 2 B) and observed their localization when tagged with YFP and produced from the chromosomal xylose-inducible promoter as a second copy (Fig. 2, C and D; and Fig. S1 A, Western blot). As expected, the full-length PopZ-YFP localized at one or both poles, depending on the cell cycle stage. Interestingly, polar accumulation was abrogated for the PopZ-YFP variants missing the H3H4 domain (Fig. 2, C and D, ΔH3H4, ΔC, and N). Conversely, all variants containing the H3H4 domain (ΔN, C, H3H4, and ΔH2), including the H3H4 domain alone, maintained the proper polar localization of PopZ (Fig. 2, C and D). Thus, the conserved 53–amino acid H3H4 domain is not only required, but also sufficient, for polar accumulation in wild-type cells.

Because wild-type cells also express a native copy of *popZ*, it was unclear whether the H3H4 domain is directly involved in pole recognition or is required for polar localization through an interaction with the wild-type PopZ already present at the poles. To discriminate between these two possibilities, we expressed the PopZ-YFP variants in a Δ*popZ* strain. Not surprisingly, the ΔH3H4, ΔC, and N variants remained diffuse in the Δ*popZ* strain (Fig. 3, A and B). The ΔH2 and ΔN variants retained their ability to localize at the poles in the absence of the native PopZ (Fig. 3, A and B), although the polar foci of ΔN-YFP were weak, unipolar, and observed in fewer cells (which we discuss later). Polar foci were also observed when ΔN was fused to the small tetracysteine (TC) tag instead of YFP and expressed in Δ*popZ* cells (Fig. 3 C), showing that the polar localization pattern was not specific to the tag. These results indicate that neither the N-terminal nor the H2 domain is absolutely required for polar localization. On the other hand, the constructs containing only the C-terminal domain (C) or part of it (H3H4) displayed a diffuse localization in all cells when PopZ was absent (Fig. 3, A and B), in contrast to their localization pattern in *popZ*$^+$ cells (Fig. 2, C and D). This localization defect was not caused by a lower protein concentration, as demonstrated by comparing cells with similar concentrations of protein variants (Fig. S1, B and C). We therefore concluded that the polar localization of the H3H4 and C variants in wild-type cells (Fig. 2, C and D) relies on their interaction with the native PopZ. Note that none of the variants, except ΔH2 (the only one with a normal localization pattern), were able to complement the cell length and stalkless phenotypes of Δ*popZ* (Fig. 3, A and D).

Our data show that the H3H4 domain does not work as a pole recognition domain per se. Instead, it likely promotes interaction between PopZ molecules. Therefore, we hypothesized that the H3H4 domain enables the oligomerization of PopZ

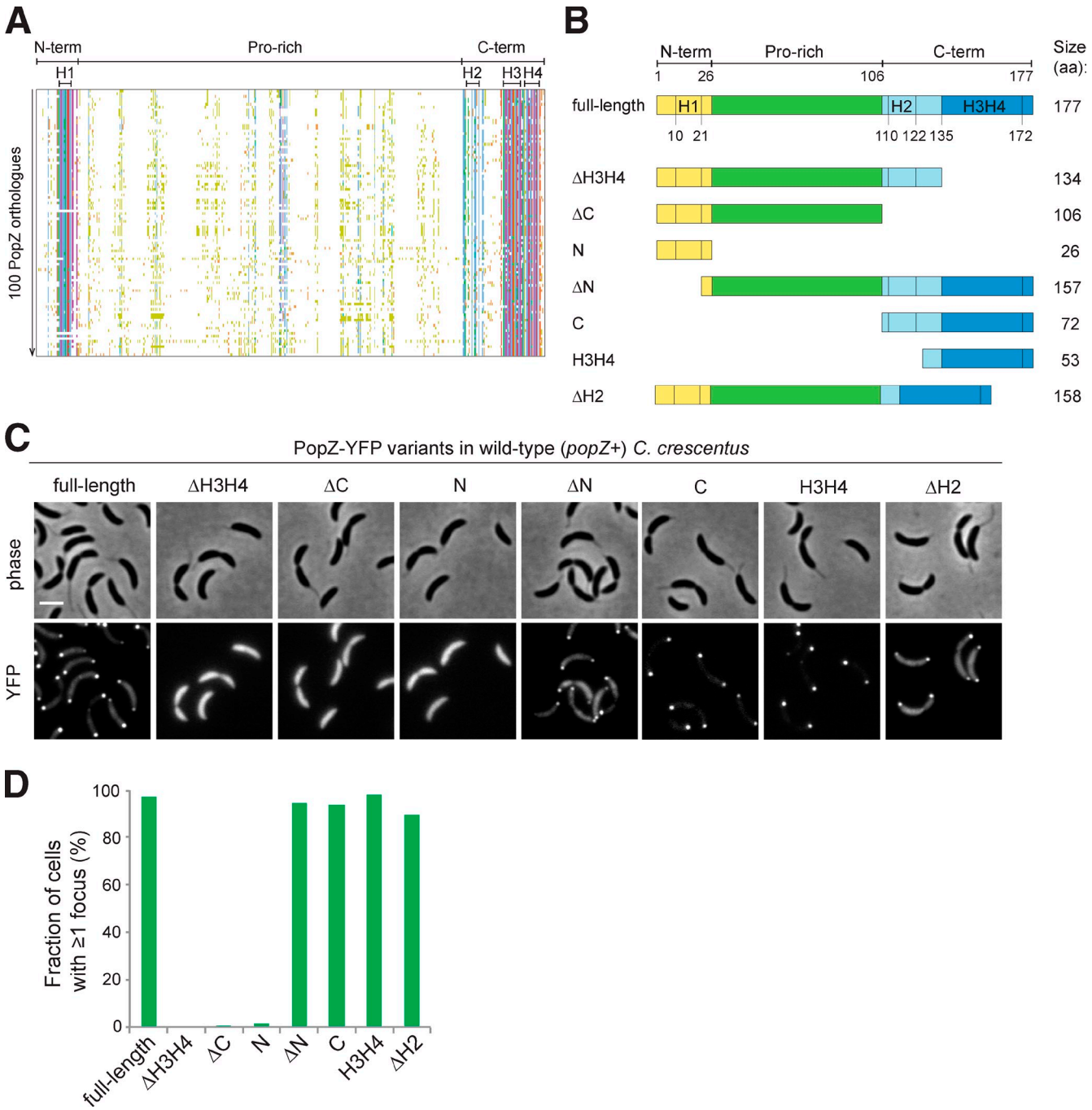

Figure 2. **The C-terminal H3H4 domain of PopZ is necessary and sufficient for polar localization in wild-type *C. crescentus* cells.** (A) Schematic overview of a multiple sequence alignment of 100 PopZ orthologues highlighting regions of conservation, displayed with Jalview using the Clustal X color scheme (Waterhouse et al., 2009). Proline (Pro) residues are all depicted in light green. The three main domains and the approximate positions of the α helices (H1–4), predicted with Jpred 3 (Cole et al., 2008), are indicated. term, terminal. (B) Schematic representation of the PopZ truncation variants. Domains, predicted α helices, and their position are indicated as well as the size of each variant (in amino acids). All regions are drawn to scale. (C) Localization of PopZ-YFP variants in *C. crescentus* cells. Synthesis of the PopZ-YFP variants was induced for 5 h in wild-type cells before imaging (phase contrast and YFP fluorescence). The YFP signal has been scaled for display. Bar, 2 µm. Strains are as follows: CJW3693 for full-length; CJW3695 for ΔH3H4; CJW3696 for ΔC; CJW3801 for N; CJW3694 for ΔN; CJW3697 for C; CJW3802 for H3H4; and CJW3816 for ΔH2. (D) YFP spots were detected from images in C. The percentage of cells with at least one focus of PopZ-YFP variant is shown. All foci were polarly localized. Number of cells counted (*n*): *n* = 765 for full-length; *n* = 701 for ΔH3H4; *n* = 803 for ΔC; *n* = 656 for N; *n* = 568 for ΔN; *n* = 726 for C; *n* = 721 for H3H4; and *n* = 941 for ΔH2. The data shown are from a representative experiment out of three repeats.

monomers. In cell extracts, oligomers of PopZ can be detected as high molecular weight species (typically doublets) on native polyacrylamide gels (Bowman et al., 2008). The full-length PopZ-YFP variants in wild-type (*popZ*$^+$) and Δ*popZ* cell extracts kept in the native state migrated as high molecular weight species (Fig. 3 E), as expected. Conversely, only forms of lower molecular weight (likely monomers) were detected when the samples were denatured in SDS (Fig. 3 E). Consistent with our hypothesis, all tested variants containing the H3H4 domain, including the H3H4 domain alone, were detected as high molecular

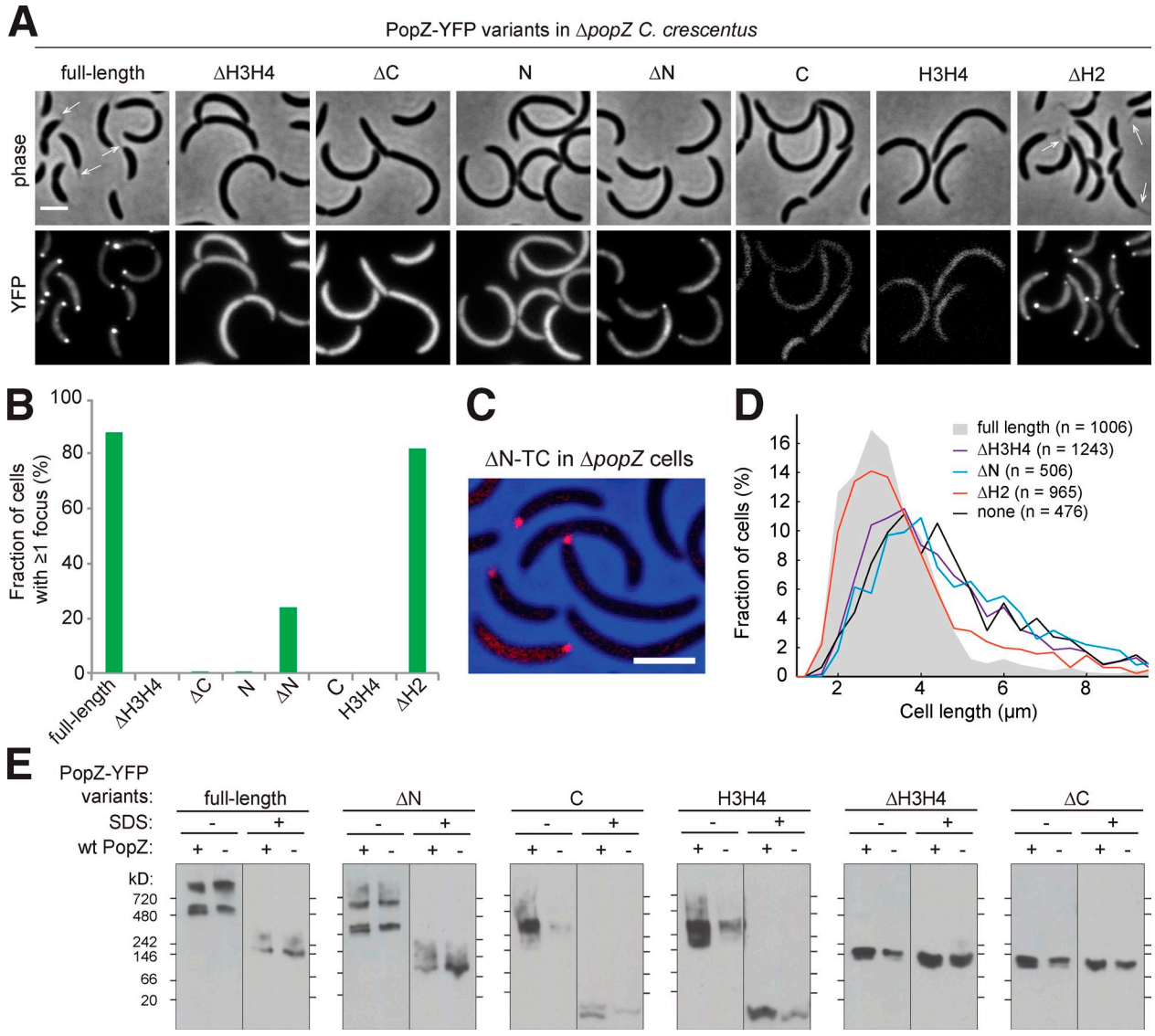

Figure 3. **The H3H4 domain mediates PopZ oligomerization.** (A) Synthesis of the PopZ-YFP variants was induced for 5 h before imaging. The YFP signal has been scaled for display. Strains are as follows: CJW3707 for full-length; CJW3709 for ΔH3H4; CJW3710 for ΔC; CJW3804 for N; CJW3708 for ΔN; CJW3711 for C; CJW3805 for H3H4; and CJW3818 for ΔH2. Arrows point at stalks. (B) YFP spots were detected from images in A. The percentage of cells with at least one focus of PopZ-YFP variant is shown. All foci were localized at the pole. Number of cells counted: 1,067 for full-length; 699 for ΔH3H4; 592 for ΔC; 448 for N; 786 for ΔN; 576 for C; 755 for H3H4; and 790 for ΔH2. The data shown are from a representative experiment out of three repeats. (C) ΔN-TC synthesis was induced in CJW4432 cells for 4.5 h before FlAsH staining and imaging. An overlay of phase-contrast and FlAsH signal (red) is shown. (D) Distribution of cell lengths for strains shown in A. (E) Western blot detection of PopZ-YFP variants after migration of whole-cell extracts in native gels. Expression of the variants was induced in Δ*popZ* (wild-type [wt] PopZ$^-$) or wild-type (wild-type PopZ$^+$) cells for 3 h. Samples were kept in a native state (SDS$^-$) or denatured (SDS$^+$) before native PAGE. Reference ticks from the NativeMark Unstained Protein Standard ladder (used in all gels) are shown. Black lines indicate that intervening lanes have been spliced out. Strains (wild-type/Δ*popZ* background) are as follows: CJW3693/CJW3707 for full-length; CJW3695/CJW3709 for ΔH3H4; CJW3696/CJW3710 for ΔC; CJW3694/CJW3708 for ΔN; CJW3697/CJW3711 for C; and CJW3802/CJW3805 for H3H4. Bars, 2 μm.

weight complexes in both *popZ*$^+$ and *popZ*$^-$ native samples (Fig. 3 E, ΔN, C, and H3H4). Furthermore, PopZ-YFP variants missing H3H4 (Fig. 3 E, ΔH3H4 and ΔC) only migrated as monomers regardless of the presence of wild-type PopZ, showing that the H3H4 domain is required for oligomerization and hence interaction with wild-type PopZ. Because these H3H4-lacking variants were unable to localize at the poles, we conclude that the H3H4 domain is necessary for PopZ oligomerization in vivo and that this oligomerization is required for polar localization.

Although necessary, oligomerization is not sufficient for polar accumulation because the H3H4 domain alone oligomerizes (Fig. 3 E) but does not display polar localization in Δ*popZ* cells (Fig. 3 A), likely because H3H4 oligomers cannot assemble into a matrix. This supposition was supported by overproduction experiments. When full-length PopZ-TC was overproduced, the FlAsH-stained matrix at the pole expanded into the cell interior, creating large fluorescent regions (Fig. S1 D), as shown previously (Ebersbach et al., 2008). In contrast, the TC-tagged H3H4 domain alone failed to form large FlAsH-stained

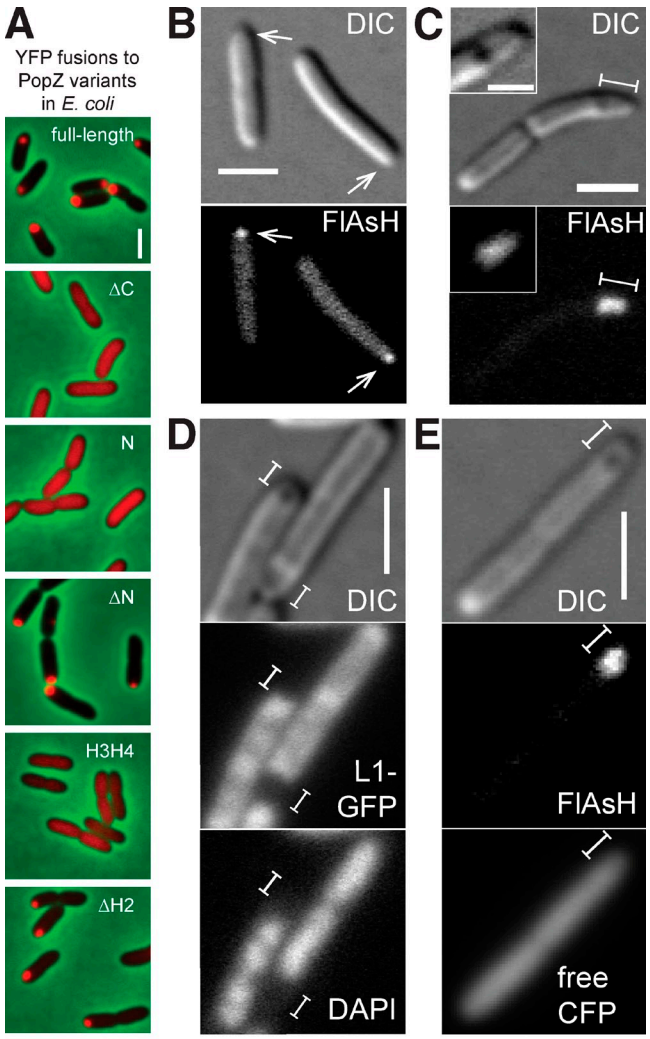

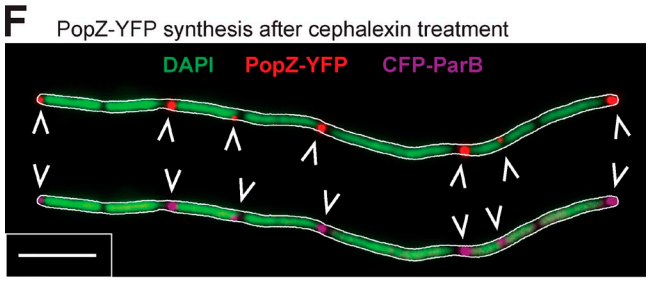

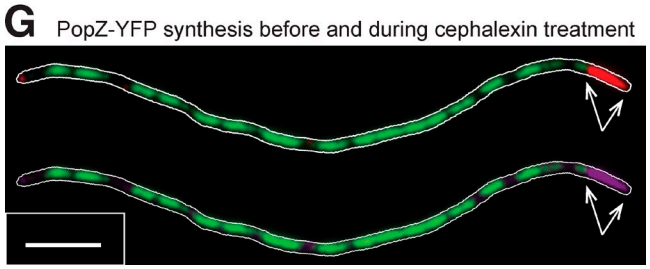

Figure 4. **PopZ assembles into a selective matrix at the pole in *E. coli*.** (A) Synthesis of YFP-tagged PopZ variants was induced for 2 h in *E. coli* cells grown in LB medium. Overlays of phase-contrast (green background) and YFP fluorescence signal (red) are shown. Strains are as follows: CJW3997 for full-length; CJW4684 for ΔC; CJW4685 for N; CJW4659 for ΔN; CJW4002 for H3H4; and CJW4001 for ΔH2. Note that all YFP fusions were at the C terminus except for ΔN, which was tagged at the N terminus because the C-terminal fusion was unstable. (B) Synthesis of PopZ-TC was induced for 3 h in CJW3991 cells. Arrows point at poles with a FlAsH-stained PopZ-TC focus. (C) Cells and conditions are the same as in B. Brackets delimit the polar LRI area visualized by DIC microscopy and labeled with FlAsH-stained PopZ-TC. The inset shows a zoomed example of a polar LRI region. (D) PopZ-TC synthesis was induced for 2 h in L1-GFP–producing CJW4673 cells before DAPI staining and imaging. Brackets delimit polar LRI areas visualized by DIC microscopy. (E) PopZ-TC production was induced for 2 h in strain CJW4744. PopZ-TC was labeled with FlAsH. Brackets delimit a polar LRI area visualized by DIC microscopy. (F) CJW3997 cells were treated with cephalexin for 2 h before induction of PopZ-YFP and CFP-ParB synthesis for 1 h. Cells were stained with DAPI before imaging. Overlays of DAPI and PopZ-YFP (top) or CFP-ParB (bottom) with the MicrobeTracker cell outline are shown. Arrowheads indicate polar and nonpolar foci. (G) PopZ-YFP synthesis was induced in CJW3997 cells for 1 h before addition of cephalexin for an additional 3 h. CFP-ParB synthesis was induced during the last hour of treatment before DAPI staining and imaging. Overlays are displayed as in F. Arrows delimit the accumulation of PopZ-YFP and CFP-ParB at one pole. Bars: (A–C [main image], D, and E) 2 µm; (C, insets) 1 µm; (F and G) 5 µm.

areas when overproduced in wild-type (*popZ*$^+$) cells (Fig. S1 D), consistent with a defect in matrix assembly. Collectively, these experiments suggest that PopZ oligomerization and matrix formation are required for polar localization.

PopZ stochastically assembles into a polar matrix of selective permeability in *Escherichia coli*

The γ-proteobacterium *E. coli*, which is evolutionary divergent from the α-proteobacterium *C. crescentus*, does not encode homologues of PopZ (or homologues of proteins that are polarly recruited by PopZ in *C. crescentus*). Interestingly, recombinant synthesis of fluorescently labeled *C. crescentus* PopZ in *E. coli* results in polar fluorescent foci (Bowman et al., 2008; Ebersbach et al., 2008). This suggests that PopZ localization does not require an extra protein anchor at the pole, as such protein would be expected to be either absent in *E. coli* or to lack a PopZ-interacting surface because of the absence of selective pressure. An alternative, more trivial explanation for this observation is that the formation of polar PopZ foci in *E. coli* is caused by protein misassembly and amorphous aggregation—as recently demonstrated for fluorescent fusions to other multimeric proteins (Landgraf et al., 2012)—and protein aggregates are known to accumulate at the cell poles (Winkler et al., 2010).

We sought to assess the relevance of the heterologous *E. coli* system by first monitoring the localization of PopZ-YFP variants in *E. coli*. Strikingly, the PopZ truncation variants that were able to form polar foci in Δ*popZ C. crescentus* cells (i.e., ΔN and ΔH2) also displayed polar accumulations in *E. coli* (Fig. 4 A). Moreover, variants that only displayed a diffuse localization pattern in Δ*popZ C. crescentus* cells (ΔC, N, and H3H4) also had a diffuse distribution in *E. coli* (Fig. 4 A). The results were confirmed by visualizing the polar PopZ constructs and H3H4 as a control, with the small TC tag and FlAsH staining instead of YFP (Fig. S1 E), showing that the localization pattern is not dependent on a bulky tag. The consistency of localization patterns between *E. coli* and *C. crescentus* provides a first line of validation of the heterologous *E. coli* system.

A second line of validation comes from our finding that not only the pole accumulation of PopZ but also the characteristics

of the PopZ matrix observed in *C. crescentus* can be recapitulated in *E. coli*. In *C. crescentus*, PopZ assembles into a matrix that is clearly distinct from amorphous aggregates (Ebersbach et al., 2008; Bowman et al., 2010). First, the mesh size of the PopZ matrix is selective by excluding DNA and ribosomes, while allowing the free diffusion of small proteins such as GFP. Additionally, when PopZ is overproduced in *C. crescentus*, the matrix expands from the pole into the cell interior and creates a region of a low refractive index (LRI) observable by differential interference contrast (DIC; Ebersbach et al., 2008) and phase-contrast microscopy (Fig. S2) because of an optical effect likely related to the ribosome exclusion (Ebersbach et al., 2008). Although FlAsH-stained PopZ-TC polarly localized in *E. coli* cells (Fig. 4 B), we observed that the FlAsH signal associated with PopZ-TC could be quite large in some *E. coli* cells as a result of PopZ-TC accumulation over multiple generations, as it expanded into the cell body to form LRI regions visible by DIC microscopy (Fig. 4 C, brackets). Using a GFP fusion to the ribosomal protein L1, we found that the polar LRI regions where PopZ accumulated were devoid of ribosomes (Fig. 4 D, brackets), which contrasts with the polar enrichment of ribosomes normally observed in *E. coli* cells (Robinow and Kellenberger, 1994). The PopZ-TC LRI areas were always found to be devoid of DAPI signal (Fig. 4 D). Conversely, free CFP showed an even distribution in PopZ-TC–producing *E. coli* cells, including the LRI regions (Fig. 4 E). Thus, the polar structure formed by PopZ in *E. coli* cells is porous and displays the same differential permeability as the PopZ matrix in *C. crescentus*. This property would not be expected from an amorphous aggregate.

Our results validate *E. coli* as an in vivo system to investigate the mechanisms underlying PopZ polar localization. They also support the notion that PopZ has the intrinsic propensity to assemble into an organized matrix at the cell poles.

An increase in PopZ concentration leads to the expansion of an existing PopZ matrix over an initiation of new assemblies

Localization of PopZ is generally unipolar in the relatively fast growing *E. coli* cells (Bowman et al., 2008; Ebersbach et al., 2008). The daughter cell that does not inherit the polar PopZ accumulation builds a new PopZ focus at either the old or new pole (Ebersbach et al., 2008), consistent with a stochastic process. If division in *E. coli* is blocked by cephalexin treatment, and PopZ synthesis is induced in the resulting filamentous cells, PopZ forms foci in any chromosome-free regions, including internucleoid regions (Ebersbach et al., 2008). Note that because internucleoid regions do not have the higher degree of membrane curvature characterizing the cell poles, these results indicate that PopZ does not localize by "sensing" membrane curvature, unlike the *Bacillus subtilis* protein DivIVA (Lenarcic et al., 2009; Ramamurthi and Losick, 2009). Interestingly, we found that if PopZ-YFP synthesis is already induced before the cephalexin treatment, PopZ continues to mostly accumulate at the pole where accumulation had already occurred before drug treatment, even when more DNA-free spaces become available within the cell body (Fig. 4 G). In both cases, PopZ accumulations efficiently recruited an exogenously produced *C. crescentus* CFP-ParB fusion (Fig. 4, F and G), supporting the functional relevance of these PopZ structures. These results indicate that PopZ can spontaneously assemble in virtually any low DNA density regions, unless a PopZ matrix is already present. Collectively, these observations support the notion that PopZ tends to assemble into a growing matrix—which offers multiple PopZ self-interaction sites—rather than initiating assemblies elsewhere. These results thus argue against the idea that a simple increase in the cellular concentration of PopZ accounts for the unipolar to bipolar localization switch observed during the *C. crescentus* cell cycle (Saberi and Emberly, 2010). Furthermore, fluorescence intensity measurements indicated that the cellular concentration of PopZ-YFP does not change during the cell cycle (Fig. S3 A). Thus, our results suggest the existence of a mechanism in *C. crescentus* that stimulates ("forces") the multimerization of PopZ at the new pole to yield a bipolar pattern.

The timing of PopZ accumulation at the new pole is tied to segregation of the ParB-*parS* complex in *C. crescentus*

We considered a role for DNA replication because blocking the initiation of DNA replication in synchronized swarmer cells has been reported to prevent the accumulation of PopZ at the new pole by an unidentified mechanism (Bowman et al., 2010). We confirmed that most cells retained a unipolar PopZ pattern after depletion of the DNA replication initiator DnaA (unpublished data). Interestingly, when cells were treated with the gyrase inhibitor novobiocin at a concentration that minimize effects on growth rate, a substantial fraction of cells (up to >60%) displayed bipolar localization of PopZ-YFP over time (Fig. 5, A and B). DNA replication initiation appeared efficiently blocked by the novobiocin treatment, as indicated by the constant low fraction of cells with two CFP-ParB foci (Fig. 5 C) and by the diffuse localization of the mCherry-tagged replisome component DnaN (Fig. 5 D), whose diffuse-to-focus localization pattern is used as a proxy for DNA replication initiation (Collier and Shapiro, 2009). Thus, our results show that a PopZ focus can appear at the new pole despite a block of DNA replication, at least in novobiocin-treated cells. Similar trends were observed when PopZ-YFP was expressed from its native promoter, although a lower fraction of cells with bipolar PopZ was observed (Fig. 5 D and Fig. S4, A and B). Neither PopZ concentration, nor cell length differences, could explain the ability of some cells to form a second PopZ focus when DNA replication is blocked (Fig. S4 C).

How can PopZ accumulate at both poles in novobiocin-treated cells? It has been previously shown that the unreplicated *parS* region often switches from the old pole to the new pole in novobiocin-treated cells in a ParA-dependent manner (Shebelut et al., 2010), reminiscent of the translocation of the replicated *parS* region that normally occurs after initiation of DNA replication. We confirmed by time-lapse microscopy that in many novobiocin-treated cells (61%, $n = 314$), the unreplicated *parS* site labeled with CFP-ParB is translocated, at least once, from one pole to the other. In all cases in which PopZ-YFP visibly accumulated at the new pole, it followed a CFP-ParB–*parS* translocation to the new pole (Fig. 5 E).

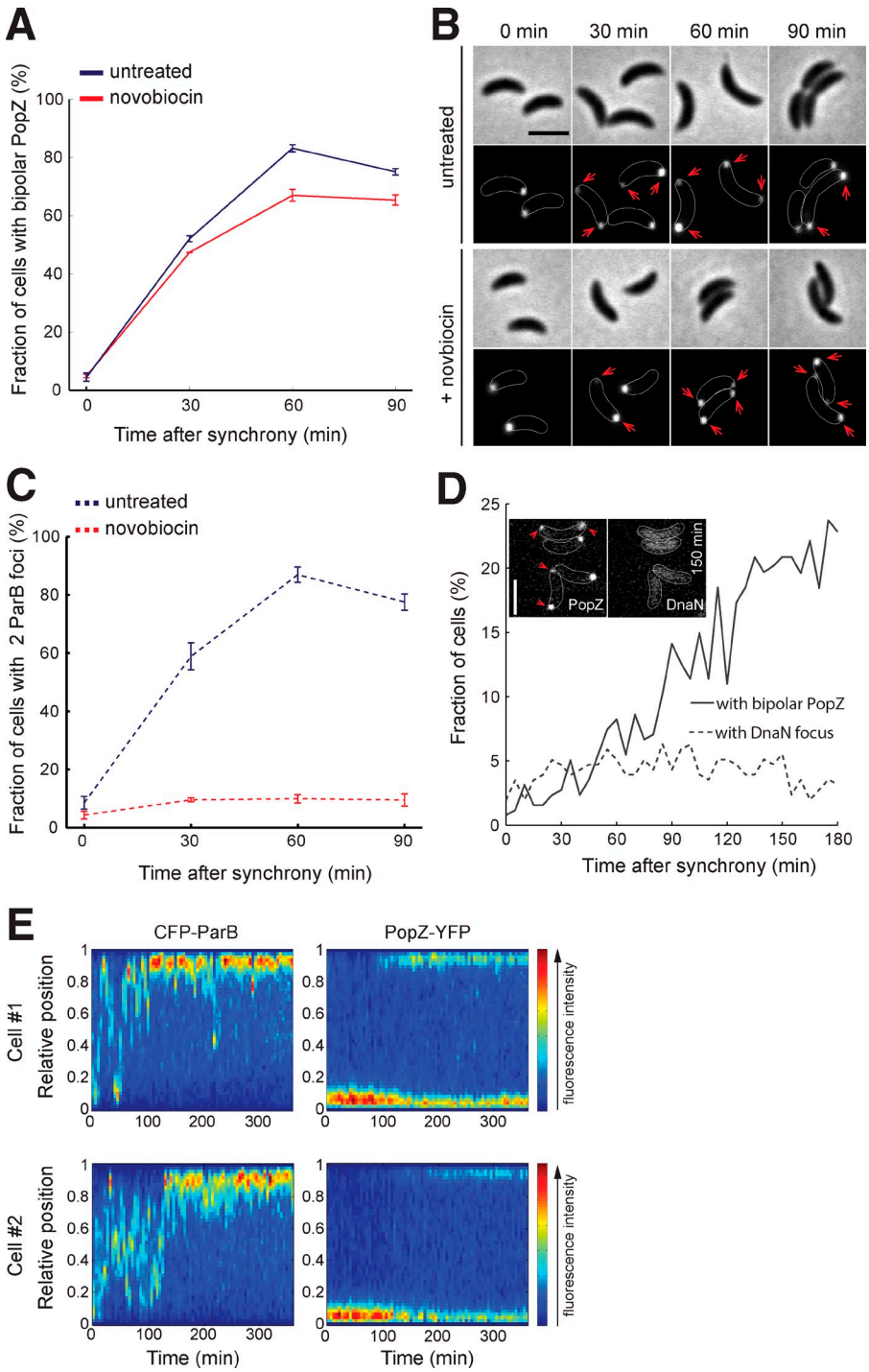

Figure 5. **Bipolar localization of PopZ can happen in the absence of DNA replication.** (A) CJW2214 cells were grown in liquid medium with xylose to induce the expression of YFP-PopZ. Swarmer cells were treated or not treated with 25 µg/ml novobiocin and imaged every 30 min. The mean fraction of cells showing bipolar YFP-PopZ localization (from three independent experiments per condition) is shown for each time point. Error bars show SEM. (B) Representative cells from one experiment described in A are shown for each time point, under untreated and novobiocin-treated conditions. Arrows point at bipolar YFP-PopZ foci. (C) CFP-ParB was imaged at each time point in the same cells as in A. The mean fraction of cells having two CFP-ParB foci (from three independent experiments per condition) is shown for each time point. Error bars show SEM. (D) Swarmer CJW4721 cells were grown on an M2G agarose pad containing 5 µg/ml novobiocin. The fraction of cells with two PopZ-YFP foci or with at least one DnaN-mCherry focus (indicative of DNA replication) is shown for each time point. Outlines and fluorescent signals of representative cells at 150 min after synchrony are shown. Arrowheads point at bipolar PopZ-YFP. (E) Swarmer CJW2237 cells were grown on an M2G agarose pad containing 5 µg/ml novobiocin. Shown are kymographs of the PopZ-YFP and CFP-ParB signals along the cell length over time from two representative cells. Relative positions of 0 and 1 represent the old pole and the new pole, respectively. Note that *C. crescentus* grows slower on agarose pads (E) than in liquid cultures (as in A). Bars, 2 µm.

These observations led us to hypothesize that the new pole accumulation of PopZ may depend on DNA segregation, rather than replication. Because, in wild-type cells, the process of *parS* segregation (that is, translocation of the duplicated *parS* locus to the new pole) is quickly completed after DNA replication is initiated (Jensen et al., 2001; Viollier et al., 2004), we sought to slow down *parS* segregation to (a) increase the time resolution at which we can distinguish replication and segregation and, therefore, (b) determine more precisely the time of appearance of PopZ at the new pole relative to both events. For this purpose, we monitored PopZ localization in a TipN-depleted (TipN$^-$) strain, in which replication of the ParB–*parS* partition complex is normal, but its segregation is slowed down (Ptacin et al., 2010; Schofield et al., 2010). We predicted that, if the timing of PopZ accumulation at the new pole was dependent on ParB–*parS* segregation, PopZ should form a focus at the new pole later in TipN$^-$ cells compared with wild-type cells. Consistent with this idea, we observed a delay in the appearance of the second PopZ-YFP focus for TipN$^-$ cells compared with TipN$^+$ cells (Fig. 6 A). This effect was also seen when using cell length instead of time as a marker of cell cycle progression, which accounts for any cell growth defect (Fig. 6 A). As expected, segregation of ParB–*parS* (labeled

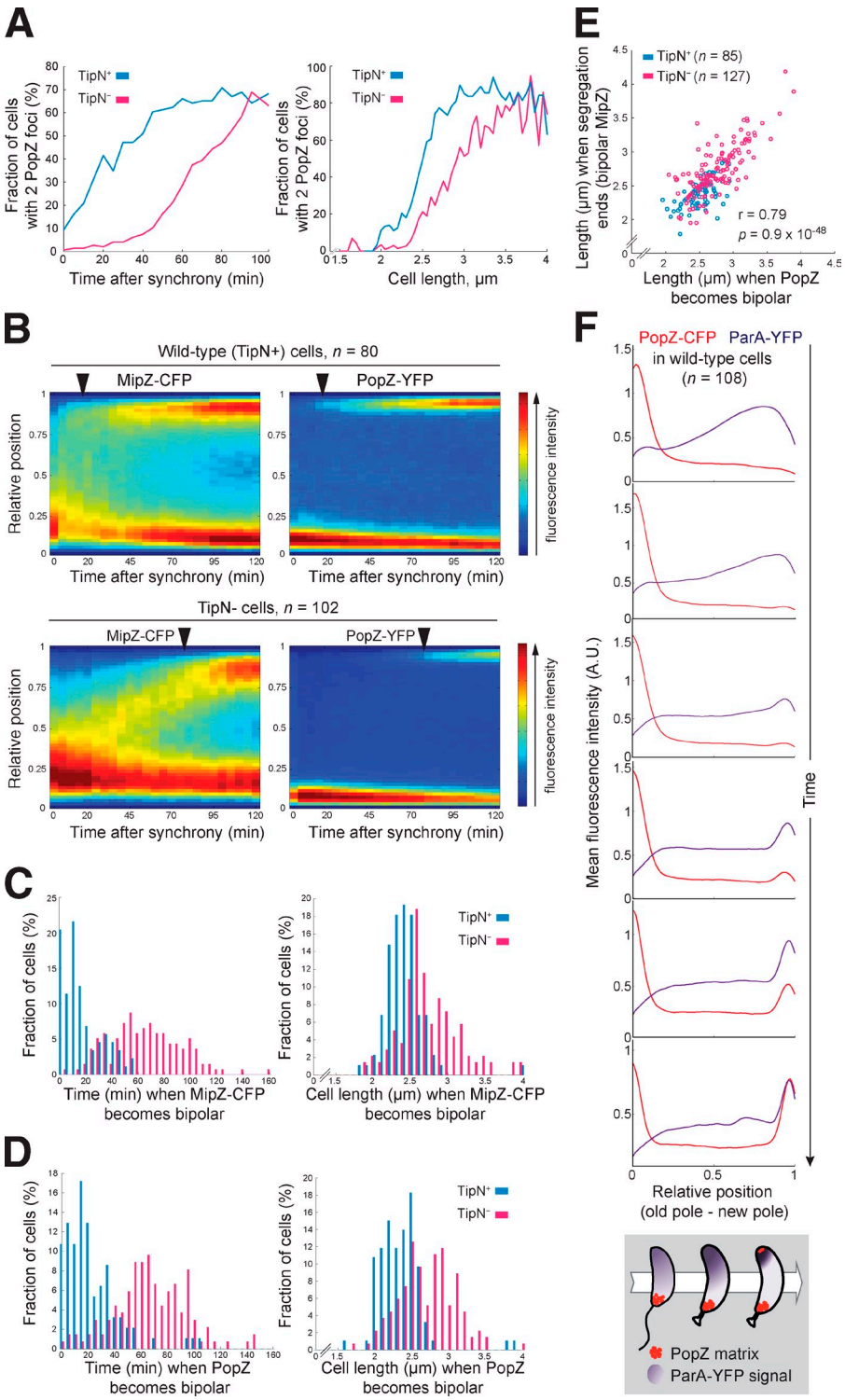

Figure 6. **Bipolar localization of PopZ correlates with the completion of *parS* segregation.** (A) CJW3544 cells were grown with (TipN$^+$) or without (TipN$^-$) xylose before synchrony. Swarmer cells were grown on M2G agarose pads with (TipN$^+$) or without xylose (TipN$^-$), and PopZ-YFP and MipZ-CFP were imaged every 5 min. (left) The fraction of cells with two PopZ-YFP foci for each time point. (right) All cells from all time points were sorted by cell length, and the fraction of cells with two PopZ-YFP foci is shown for each bin of 0.05 µm. (B) Kymographs of the MipZ-CFP (proxy for *parS*) and PopZ-YFP signal intensity profiles along the cell length over time, averaged for the population of TipN$^+$ cells and TipN$^-$ cells imaged in A. Total cell numbers are indicated (*n*). Relative position of 0 and 1 represent the old pole and the new pole, respectively. Arrowheads indicate the appearance of PopZ-YFP at the new pole. (C) Distribution of the time after synchrony (left) or the cell length (right) at which MipZ-CFP (*parS*) reaches the new pole in each cell population imaged in A. (D) Distribution of the time after synchrony (left) or of cell length (right) when a second PopZ-YFP focus is first detected. (E) For each TipN$^+$ and TipN$^-$ cell imaged in A, the cell length at which PopZ-YFP (x axis) or MipZ-CFP (y axis) reached the new pole was recorded. Each dot represents one cell. Correlation coefficient (r), p-value, and cell counts (*n*) are indicated. (F) PopZ-CFP and ParA-YFP were imaged in synchronized cells (CJW4626; *n*: cell counts) grown on an M2G agarose pad. The mean fluorescence intensity profile along the cell length is shown for each fusion protein during cell cycle progression. PopZ and ParA as seen by epifluorescence microscopy are represented on schematics for three representative steps during the cell cycle.

with MipZ-CFP, which binds ParB; Thanbichler and Shapiro, 2006) was slowed down in TipN$^-$ cells compared with TipN$^+$ cells, as indicated by mean kymographs of the MipZ-CFP signal (Fig. 6 B, left) for each cell population. The delay in MipZ-CFP segregation to the new pole in TipN$^-$ cells was accompanied by a comparable delay in PopZ-YFP accumulation at that pole (Fig. 6 B, right, arrowheads). Thus, at least at the population level, our data suggested a temporal coupling between the segregation of ParB–*parS* and the localization of PopZ at the new pole.

Next, we asked whether this coupling was also manifest at the single-cell level. This was relevant because cells complete ParB–*parS* segregation at quite variable times after synchrony (Fig. 6 C, left). Cell-to-cell variability is even wider in the TipN$^-$ population (Fig. 6 C, left), as ParB–*parS* translocation is more erratic in this background (Ptacin et al., 2010; Schofield et al., 2010). These broad distributions were not the result of synchronization imperfections or growth rate differences among cells because they were also observed when we considered the

cell length (instead of the time) at which ParB–*parS* segregation is completed (Fig. 6 C, right). Strikingly, the variability of PopZ focus formation at the new pole in time and cell length mirrored that of *parS* segregation, for both $TipN^+$ and $TipN^-$ populations (Fig. 6 D). Furthermore, we found a strong positive correlation between the cell length—used to follow cell cycle progression—at which PopZ appears at the new pole and the cell length when segregation ends in individual cells (Fig. 6 E). On the other hand, the correlation was much poorer between DNA replication initiation and the new pole localization of PopZ in $TipN^-$ cells (Fig. S4 D), in which replication initiation and segregation are well separated in time.

Moreover, the reported effect of MreB inhibition on the new pole accumulation of PopZ (Bowman et al., 2008) could be fully explained by a delay in chromosome segregation, which is caused by a general slowdown in growth and cell cycle progression (Fig. S4, E–H; Takacs et al., 2010; Sliusarenko et al., 2011). There again, the dynamics of PopZ localization and ParB–*parS* translocation were very well correlated at the single-cell level (Fig. S4 H).

A PopZ variant lacking the N-terminal domain has a unipolar localization pattern and is deficient in the polar recruitment of ParA and ParB

How could the translocation of ParB–*parS* to the new pole lead to PopZ accumulation at that location? This DNA translocation process involves two proteins, ParB and ParA (Mohl and Gober, 1997; Ptacin et al., 2010; Schofield et al., 2010; Shebelut et al., 2010). The presence of the ParB focus (associated with *parS*) at the new pole correlates with the appearance of a PopZ focus at the new pole (Fig. 6 E). Similarly, ParA, whose concentration gradient shifts toward the new pole as ParB–*parS* segregation proceeds (Schofield et al., 2010), increases its local concentration in the vicinity of the new pole at the time when a second PopZ focus starts building at that location (Fig. 6 F). Thus, the unipolar to bipolar transition of PopZ correlates with both the translocation of ParB–*parS* and the new pole accumulation of ParA. PopZ is known to interact with both ParB (Bowman et al., 2008; Ebersbach et al., 2008) and ParA (Schofield et al., 2010), although the reason for the PopZ–ParA interaction was not clear. It is important to note that not all PopZ molecules localize at the poles; there is a diffusing cytoplasmic pool of PopZ (Bowman et al., 2008), which we estimate to be ∼40% of the total PopZ proteins per cell based on our fluorescence intensity measurements (Fig. S3 B). Therefore, we speculated that a high concentration of either ParB or ParA (or both) may, through interaction with PopZ, increase the local concentration of diffusing PopZ to a level sufficient to nucleate PopZ assembly into a matrix in the low DNA density region of the new pole.

This hypothesis predicts that a PopZ mutant unable to interact with ParA and/or ParB in *C. crescentus* would be unable to display bipolar localization; instead, it would preferentially accumulate at one pole only through stochastic multimerization, as observed in *E. coli*. Interestingly, the foci of the TC or YFP-tagged ΔN variant were always unipolar, not only in *E. coli* (Fig. 4 A) but also in *C. crescentus* in the absence of native PopZ (Fig. 3, A and C). Using three different assays, we found that the N-terminal domain of PopZ (missing in the ΔN variant) is required for in vivo interaction of PopZ with ParA and ParB, consistent with the hypothesis that ParB and/or ParA are involved in bipolar localization of PopZ.

In our first assay, we took advantage of a DNA binding–deficient variant of ParA, $ParA_{R195E}$, which localizes predominantly at the poles in wild-type *C. crescentus* cells (Ptacin et al., 2010; Schofield et al., 2010) but is evenly distributed in the cytoplasm of Δ*popZ* cells, allowing for a straightforward monitoring of ParA–PopZ interaction (Schofield et al., 2010). As expected, polar $ParA_{R195E}$-CFP foci were observed in a large fraction (58.4%) of Δ*popZ* cells producing full-length PopZ-YFP (Fig. 7 A), and virtually all of these foci (99.8%) colocalized with a polar PopZ-YFP focus. However, the PopZ variant lacking the N-terminal domain failed to recruit $ParA_{R195E}$-CFP as $ParA_{R195E}$-CFP only displayed a diffuse pattern when ΔN-YFP was produced (Fig. 7 A). Because the polar ΔN-YFP foci are relatively weak in Δ*popZ* cells (Fig. 3 A), our second interaction assay examined the localization of $ParA_{R195E}$-CFP or CFP-ParB in Δ*popZ* cells overproducing ΔN-TC, in which case clear polar accumulations of ΔN-TC can be visualized by FlAsH staining (Fig. 7, B and C; and Fig. S5, A and B). $ParA_{R195E}$-CFP was evenly distributed throughout ΔN-TC–producing cells, without the clear enrichment normally seen in PopZ-TC–rich regions (Fig. 7 B). Similarly, the ΔN-TC–rich regions failed to recruit CFP-ParB, unlike the wild-type PopZ-TC–rich regions (Fig. 7 C). The unipolar localization pattern of ΔN or its loss of interaction with ParA and ParB is not caused by a major self-assembly defect, as this ΔN variant can assemble into a porous matrix upon overproduction (Fig. S5, A and B). Our third interaction assay was based on the observation that PopZ can recruit *C. crescentus* ParB and $ParA_{R195E}$ at the cell pole in *E. coli*, whereas these proteins display a diffuse localization pattern without PopZ (Bowman et al., 2008; Ebersbach et al., 2008; Schofield et al., 2010). In contrast to the full-length PopZ-YFP, YFP-ΔN foci were unable to recruit $ParA_{R195E}$-CFP (Fig. 7 D) and CFP-ParB (Fig. 7 E). Thus, all three tests show that the N-terminal domain of PopZ is required for interaction with both ParA and ParB. The inability of the ΔN variant to accumulate at both poles (Fig. 3, A and C) supports the hypothesis that an interaction with ParA, ParB, or both is important for bipolar localization of PopZ.

The accumulation of PopZ at the new pole is associated with the condensation of the ParA concentration gradient at the new pole region

Both ParA and ParB are essential for viability in *C. crescentus* (Mohl and Gober, 1997), and their depletion would result in cell filamentation (Mohl et al., 2001), which presents challenges in experiment design and interpretation for studying whether ParA or ParB affects PopZ localization pattern. Therefore, we took advantage of a dominant-negative variant of ParA, $ParA_{K20R}$, whose production in wild-type (*parA*$^+$) cells results in the stalling of the ParB–*parS* complex roughly halfway across the cell (Toro et al., 2008; Shebelut et al., 2010), whereas a ParA accumulation still occurred at the new pole (Fig. 7, G and H).

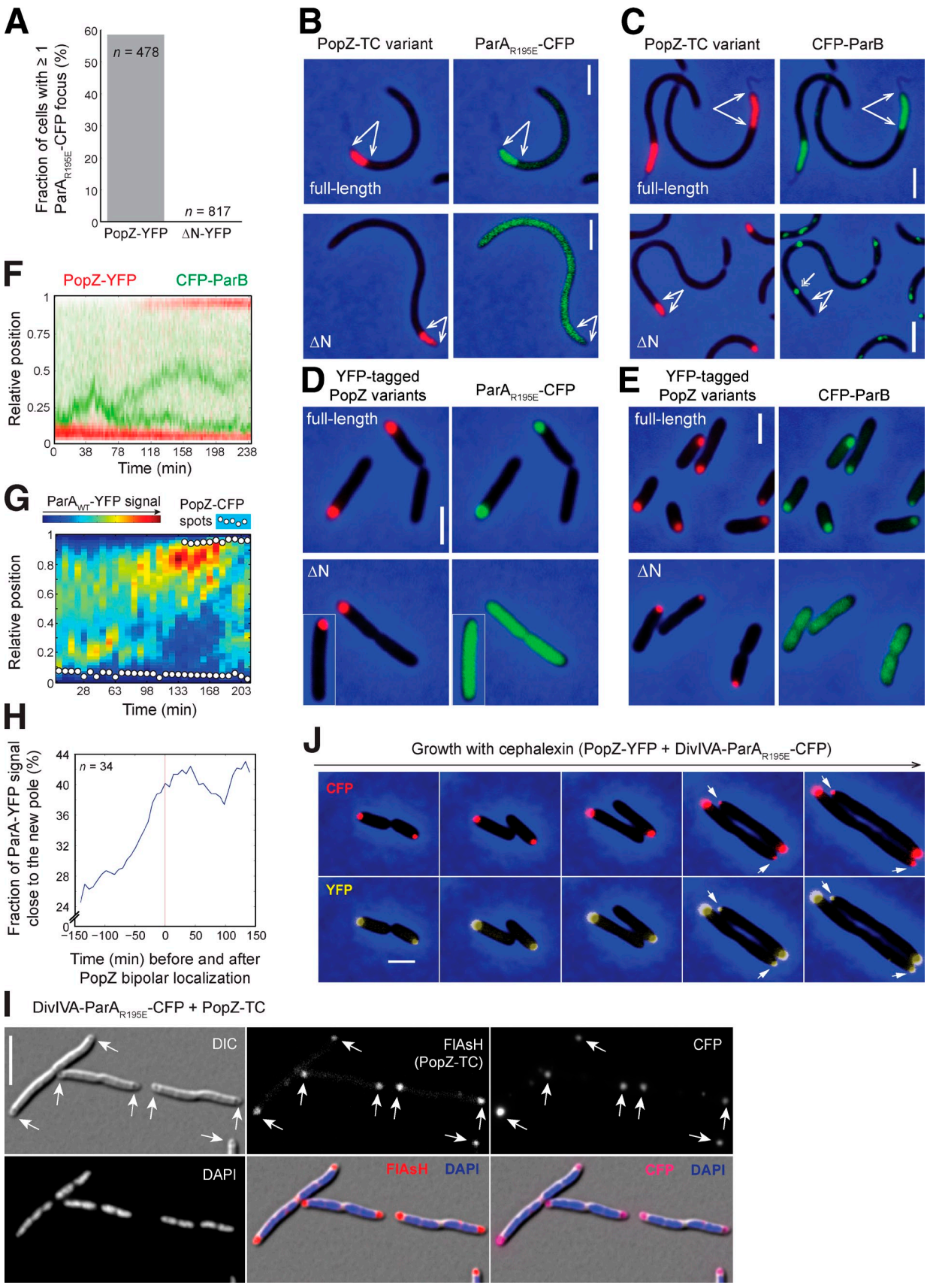

Figure 7. **ParA mediates spatiotemporal control of PopZ localization.** (A) The synthesis of PopZ-YFP variants and ParA$_{R195E}$-CFP was induced for 5 and 2 h, respectively. The bar graph shows the fraction of cells with ParA$_{R195E}$-CFP spots in *C. crescentus* cells producing PopZ-YFP (CJW4769) or ΔN-YFP (CJW4770). Cell counts (*n*) are as follows: 456 out of 478 CJW4769 cells and 137 out of 817 CJW4770 cells had at least one PopZ-YFP focus. The data

We found that PopZ-YFP retains the ability to form a second focus under these conditions (Fig. 7 F), indicating that the presence of a ParB focus at the new pole is not required for the accumulation of PopZ at that location. In some $ParA_{K20R}$-producing cells, CFP-ParB–*parS* eventually reached the new pole, but even then, the new pole accumulation of PopZ-YFP was temporally uncoupled from the completion of CFP-ParB–*parS* segregation (Fig. S5 C). In contrast, the new pole accumulation of PopZ-CFP under the same $ParA_{K20R}$-producing conditions was still correlated with an accumulation of $ParA_{WT}$-YFP in the new pole region at both the single-cell (Fig. 7 G) and the population levels (Fig. 7 H). Thus, although the new pole localization of PopZ-YFP can occur independently of the presence of ParB–*parS* at the new pole, it is concomitant with ParA accumulation in that region of the cell.

These results, together with the observation that a loss of ParA interaction is associated with a loss of bipolar localization (Fig. 3, A and C; and Fig. 7, A–E), suggest that the cell cycle–regulated accumulation of PopZ at the new pole is promoted by ParA accumulation during ParB–*parS* segregation. In other words, the ParA accumulation in the new pole region would contribute to locally increase PopZ concentration in this area, which, in turn, would raise the probability of PopZ to self-interact and to nucleate its polymerization into a matrix.

An artificially induced accumulation of ParA is sufficient to promote the initiation of PopZ matrix assembly in vivo

Reconstituting such temporally and spatially controlled reactions in vitro would be technically very difficult and would not assess the dynamics that take place within the physical limits of a cell. Therefore, we turned to the *E. coli* system—which lacks the cell cycle control of PopZ localization—and asked whether the localization of PopZ in *E. coli* could be altered by inducing ParA accumulation at defined locations within the cell.

To do this, we fused $ParA_{R195E}$-CFP to *B. subtilis* DivIVA, a protein known to accumulate at the poles when produced in *E. coli* (Edwards et al., 2000; Ding et al., 2002) through membrane curvature recognition (Lenarcic et al., 2009; Ramamurthi and Losick, 2009). This fusion resulted in an artificial accumulation of $ParA_{R195E}$-CFP at both poles of cephalexin-treated *E. coli* cells (Fig. 7 I and Fig. S5E), similar to a DivIVA-GFP fusion (Fig. S5 D). Normally (i.e., in the absence of the DivIVA-$ParA_{R195E}$-CFP fusion), induction of PopZ in cephalexin-treated *E. coli* cells results in PopZ matrix formation in any DNA-free regions, including between nucleoids (Fig. 4 F; Ebersbach et al., 2008). In contrast, when DivIVA-$ParA_{R195E}$-CFP was present at both poles, induction of PopZ-TC synthesis primarily resulted in FlAsH-stained LRI regions (indicating a PopZ-TC matrix) at the poles (Fig. 7 I, arrows), always colocalizing with the DivIVA-anchored $ParA_{R195E}$-CFP signal. The change in PopZ localization pattern was associated with the ParA accumulations and not with the presence of DivIVA as shown by the prominence of PopZ matrix formation between nucleoids in cells producing DivIVA fused to a control protein (VirB10; Fig. S5 F). Thus, an accumulation of the PopZ-interacting protein ParA at both cell poles can promote ("seed") the formation of a PopZ matrix at these locations.

In separate experiments, PopZ-YFP synthesis was only induced for 15 min before imaging under conditions of *popZ-yfp* repression to examine whether PopZ-YFP localization can change in response to a local increase in ParA concentration even in the absence of new PopZ synthesis. In some *E. coli* cells (typically cells recently generated from a division initiated before cephalexin treatment), DivIVA-$ParA_{R19E}$-CFP (under continuous expression) was found at only one pole and then accumulated at the opposite pole over time (Fig. 7 J). In these cells, PopZ-YFP (in the absence of new synthesis) switched from a unipolar to bipolar localization pattern, after the DivIVA-anchored $ParA_{R195E}$-CFP pattern (Fig. 7 J). This was not observed in cells producing DivIVA-VirB10, in which PopZ-YFP remained exclusively unipolar for the duration of the experiment (Fig. S5 G). Hence, a ParA accumulation is sufficient to promote the assembly of a PopZ matrix at the opposite pole, recapitulating what is observed in *C. crescentus*.

Discussion

Although many proteins that localize are known to multimerize (Rudner and Losick, 2010), the importance of multimerization in protein localization had not been examined. Collectively, our data suggest that not only protein multimerization can result in polar localization (Fig. 8 A) but also that this otherwise

shown are from a representative experiment out of two repeats. (B) Overproduction of PopZ-TC or ΔN-TC was induced for 5 h in CJW4845 or CJW4846 *C. crescentus* cells, respectively, and $ParA_{R195E}$-CFP synthesis was induced for 2 h, before FlAsH staining. Arrows indicate the location of the PopZ-TC or ΔN-TC–rich area. (C) PopZ-TC (CJW4746) or ΔN-TC (CJW4745) was imaged with FlAsH after overproduction for 5 h in *C. crescentus* cells. Arrows are displayed as in B. The double arrow points at one CFP-ParB focus. (D) PopZ-YFP variants and $ParA_{R195E}$-CFP were imaged in *E. coli* after induction, for 2 and 1 h, respectively. Strains are as follows: CJW4835 for full-length and CJW4836 for ΔN. Insets indicate that the cell was imaged on a different field of view. (E) PopZ-YFP variants and CFP-ParB were imaged after 2 h of induction in *E. coli* cells grown in LB. Strains are as follows: CJW3997 for full-length and CJW4659 for ΔN. (F) Kymograph of CFP-ParB and PopZ-YFP in a representative $ParA_{K20R}$-producing *C. crescentus* cell. Swarmer cells (CJW4441) were imaged every 2 min. (G) Swarmer *C. crescentus* cells (CJW4613) producing $ParA_{K20R}$ were imaged every 7 min. The kymograph of the ParA-YFP signal is shown for a representative cell, along with the relative position of the PopZ-CFP foci (white circles). (H) Mean fraction of the ParA-YFP signal located in the vicinity of the new pole before and after the formation of a second PopZ-CFP focus. The time when two PopZ-CFP spots were first detected was defined as time 0 for each cell from the experiment described in G. The fraction of ParA-YFP signal in the new pole-proximal quarter of the cell was averaged for all cells at each time point using time 0 as a reference (red line). (I) *E. coli* cells (CJW4917) producing DivIVA-$ParA_{R195E}$-CFP were grown in M9 + glucose at 30°C and treated with cephalexin for 1 h before induction of PopZ-TC synthesis by washing the cells for 30 min in M9 + glycerol containing arabinose. Cells were first stained with FlAsH for 30 min and then with DAPI before imaging. Arrows point to LRI regions. (J) *E. coli* cells (CJW4918) producing DivIVA-ParAR195E-CFP were grown in M9 + glucose, washed for 15 min in M9 + glycerol containing arabinose to briefly induce the synthesis of PopZ-YFP, and washed in M9 + glucose for 15 min before growth and time-lapse imaging on an M9 + glucose pad (repression of *popZ-yfp* expression) containing cephalexin. Representative cells are shown for selected time points. Arrows point to new foci. Bars, 2 µm.

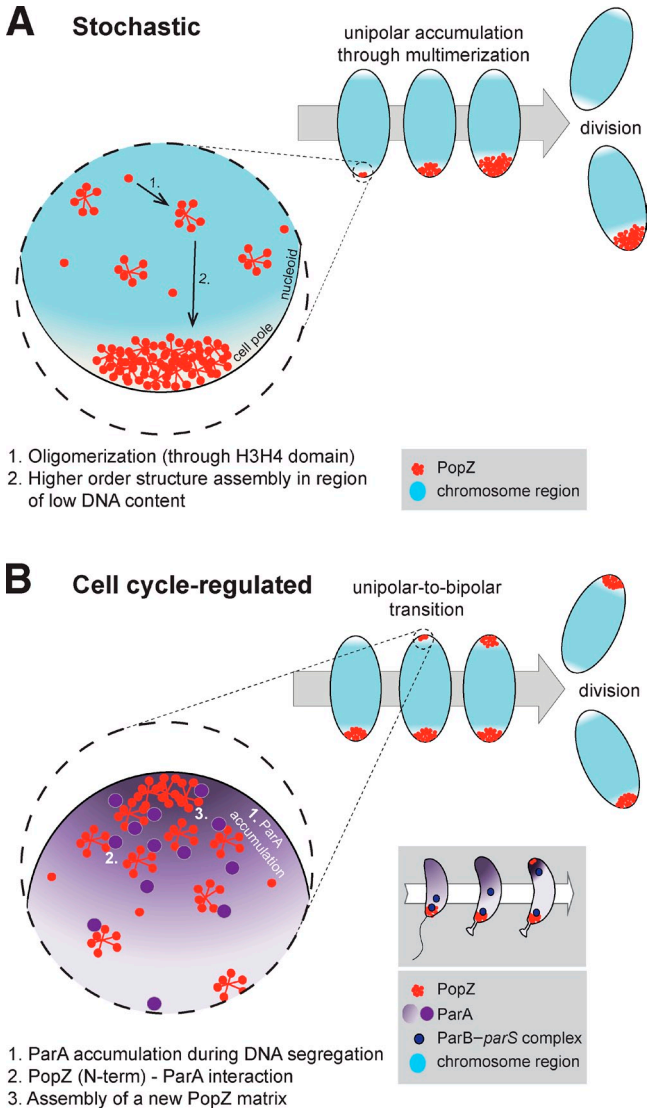

Figure 8. **Model for uncontrolled and cell cycle–controlled pole localization.** (A) Accumulation of a self-assembling protein (here PopZ) through multimerization in favorable regions, such as poles as a result of their low DNA content, is a stochastic process that leads to the expansion of the protein structure (PopZ matrix) at one pole. (B) Spatial and temporal regulation of the spontaneous multimerization process in A can be achieved through coupling with a cell cycle event (ParA-dependent ParB–*parS* segregation) that involves the local concentration of an interacting protein (ParA). Accumulation of the protein partner (ParA) results in a local increase in the concentration of diffusing self-assembling proteins (PopZ oligomers) to a level that promotes and sustains assembly into a higher-order structure (PopZ matrix) where and when the cell cycle event takes place. In the case of PopZ, a coupling with the ParA-dependent segregation of ParB–*parS* allows for the controlled assembly of a PopZ matrix at the new pole in time to capture the partitioning ParB–*parS* complex. N-term, N-terminal.

stochastic multimerization can be controlled by a cell cycle event (Fig. 8 B) to obtain both spatial and temporal control of protein localization. In this model, the two conserved domains of PopZ play distinct roles. Through its C-terminal H3H4 domain, PopZ self-assembles into oligomers, which are the building blocks of the PopZ matrix (Fig. 8 A). In the absence of a preexisting seed (an inherited PopZ matrix), PopZ multimerization into a matrix is favored in essentially any chromosome-free regions (the cell poles in normal cells). Computational simulations show that entropy alone can explain this nucleoid exclusion effect (Saberi and Emberly, 2010). Once a PopZ matrix is initiated or inherited (i.e., through division), it continues to grow through protein multimerization (Fig. 8 A). This is in agreement with the diffusion-capture mechanism deduced from PopZ-YFP single-molecule experiments (Bowman et al., 2008), except that the unidentified polar anchor that captures the soluble diffusing PopZ oligomers is the already established growing PopZ matrix. We propose that spatial and temporal control can be added to this spontaneous multimerization process to produce a defined localization pattern during the cell cycle (Fig. 8 B). This would be achieved through coordination with the ParA-dependent segregation of the partition ParB–*parS* complex. Mutant analysis show that ParA exists in two forms inside cells, a DNA-bound dimer and a free monomer (Ptacin et al., 2010; Schofield et al., 2010). The concentration of both forms increases at the new pole region as ParB–*parS* translocation proceeds. Because PopZ has affinity for both forms of ParA (Schofield et al., 2010), their accumulation during segregation results in a local increase in the concentration of cytoplasmic PopZ oligomers through interaction with the conserved N-terminal PopZ domain. This, in turn, promotes the assembly of a new PopZ matrix at the right place and time to anchor the sister chromosome.

In this model, the mechanistic principle is simple; the cell exploits a molecular asymmetry that is inherently associated with a cell cycle event to modulate the local concentration and thereby assembly of a protein. This organizing principle may represent a widespread strategy to produce precise localization patterns in time and space.

Materials and methods

Culture conditions

Synchrony, conjugation, transformation, and transduction with the bacteriophage ΦCR30 were performed as previously described (Ely, 1991). For all experiments, cells were harvested from exponentially growing cultures. *C. crescentus* strains were grown at 30°C in the defined minimal M2G medium (0.87 g/liter Na_2HPO_4, 0.54 g/liter KH_2PO_4, 0.50 g/liter NH_4Cl, 0.2% [wt/vol] glucose, 0.5 mM $MgSO_4$, 0.5 mM $CaCl_2$, and 0.01 mM $FeSO_4$) unless otherwise stated or in rich PYE medium (2 g/liter bactopeptone, 1 g/liter yeast extract, 1 mM $MgSO_4$, and 0.5 mM $CaCl_2$) when indicated. Unless otherwise stated, *E. coli* strains were grown at 37°C in the defined minimal M9 medium (12 g/liter $Na_2HPO_4 \cdot 7H_2O$, 6 g/liter KH_2PO_4, 1 g/liter NaCl, 2 g NH_4Cl, 1 mM $MgSO_4$, 0.067% casamino acids, 0.2% glycerol, and 1 mg/liter thiamine) containing 0.2% of glycerol or 0.2% glucose (when indicated) for optimal repression of P*ara*. *E. coli* cells were grown in Luria Bertani (LB)–rich medium (10 g/liter NaCl, 5 g/liter yeast extract, and 10 g/liter tryptone) when indicated. When appropriate, media were supplemented with antibiotics at the following concentrations (µg/ml in liquid/solid medium for *C. crescentus* strains; µg/ml in liquid/solid medium for *E. coli* strains): ampicillin (10/50; 100/200), chloramphenicol (2/5; 20/30), kanamycin (5/20; 50/50), nalidixic acid (15/20; 15/20), gentamycin (2/5; 15/20), spectinomycin (25/100; 50/50), and streptomycin (5/5; 30/30). Cephalexin was used at a final concentration of 10 µg/ml. Novobiocin solutions were always prepared fresh and used at the indicated concentrations in M2G medium or M2G agarose pads. When applicable, xylose was added to the culture medium of *C. crescentus* strains at a final concentration of 0.03% to induce expression from the P*xyl*, or 0.3% for overexpression from the pJS14-based vectors. Vanillic acid was used at 0.5 mM for induction of expression from the P*van*. For TipN depletion, cells were grown without xylose in the medium, starting from the preculture. To induce the synthesis of $ParA_{K20R}$ fusions, cells were grown in the presence of xylose 0.03% for 1–1.75 h before synchrony. For induction of expression from the pBAD33 vectors in *E. coli*, arabinose was added to a final concentration of 0.02%. 1 mM IPTG was used to induce expression from the P*lac* in *E. coli*.

Plasmids construction

Plasmids pCFPC-1, pCFPC-4, pCHYC-1, pXYFPC-2, pXCHYC-2, pXTCYC-2, pXYFPN-2, and pVCFPC-4 are described in Thanbichler et al. (2007).

pXYFPC-2–based plasmids. The following *popZ* variants were amplified from a CB15N colony using the primers indicated between parentheses: full-length (CJW1733 + CJW1734); ΔH3H4 (CJW1733 + CJW1741); ΔC (CJW1733 + CJW1739); N (CJW1733 + CJW1742); ΔN (CJW1740 + CJW1734); C (CJW1737 + CJW1734); and H3H4 (CJW1744 + CJW1734). The sequence coding the ΔH2 variant was generated by joint PCR. A CB15N colony was used as a template for the amplification of two initial fragments using primers CJW1733 + CJW1745 and CJW1746 + CJW1734. Those fragments were then mixed and used as template for a joint PCR using primers CJW1733 + CJW1734 to generate the *popZΔH2* product. PCR products were digested with KpnI and EcoRI and ligated with pXYFPC-2 cut with the same enzymes. Thus, three PopZ variants have C-terminal deletions: ΔH3H4 and ΔC variants lack portions of the C terminus starting from the H3 helix (residue 135) or the beginning of the C-terminal domain (residue 107), respectively, whereas the N variant is limited to the N-terminal domain (residues 1–26). N-terminal truncations affect three other variants (a start codon adds a methionine at the N terminus of each variant): ΔN lacks the first 21 residues including the H1 helix, C is missing the N-terminal and the proline-rich domains, thus leaving the C-terminal domain only, whereas H3H4 only retains part of the C-terminal domain starting at residue 126, thus containing the H3H4 helices but excluding the H2 helix. ΔH2 is missing a part of the C terminus between residues 110 and 125 that covers the helix 2.

pXTCYC-2–popZΔN. *popZΔN* was amplified from pXYCPC-2—popZΔN using primers CJW1740 and CJW1734, digested with KpnI and EcoRI, and ligated with pXTCYC-2 cut with the same enzymes.

pJS14-pxyl–based plasmids. *popZ-TC* variants were amplified using the following templates and primers: full-length (CB15N colony; CJW1747 + CJW1748); ΔN (CB15N colony; CJW1749 + CJW1748); and H3H4 (CB15N colony; CJW1750 and CJW1748). PCR products were digested with NdeI and HindIII and ligated with pJS14-pxyl, which was cut out from pJS14-pxyl-popZ using the same enzymes. To construct pJS14-pxyl-popZ, *popZ* was cut out from pXYFPC-2–popZ using NdeI and EcoRI. *pxyl* was cut out of pRW432 (cloning vector containing the *pxyl* promoter; gift from R. Wright, Stanford University, Stanford, CA) using BamHI and NdeI. The digested *popZ* and *pxyl* were inserted by triple ligation into pJS14 (medium copy pBBR1-derived broad host range vector; gift from J. Skerker, University of California Berkeley, Berkeley, CA) cut with EcoRI and BamHI.

pBAD33-based plasmids. For C-terminal TC fusions, *popZ-TC* variants were amplified from the following templates using the indicated primers: full-length (CB15N colony; CJW1747 + CJW1748); ΔH2 (CJW3818 colony; CJW1747 + CJW1748); and H3H4 (CB15N colony; CJW1750 + CJW1748). Amplification products were digested with NdeI and HindIII and ligated with pBAD33 cut out from pBAD33-popZ-TC (plasmid from CJW2269; Ebersbach et al., 2008) by the same enzymes. For pBAD33-TC-popZΔN, *TC-popZΔN* was amplified from a CB15N colony using primers CJW1752 + CJW1753, digested with NdeI and HindIII, and ligated with pBAD33 cut out from pBAD33-popZ-TC (this study) by the same enzymes. For C-terminal YFP fusions, *popZ-yfp* variants were amplified from the following template vectors using the indicated primers: full-length (pXYFPC-2–popZ; CJW1747 + CJW1754); ΔH2 (pXYFPC-2–popZΔH2; CJW1747 + CJW1754); H3H4 (pXYFPC-2–popZH3H4; CJW1750 + CJW1754); ΔC (pXYFPC-2–popZΔC; CJW1747 + CJW1754); and N (pXYFPC-2–popZN; CJW1747 + CJW1754). Amplification products were digested with NdeI and HindIII and ligated with pBAD33 cut out from pBAD33-popZ-TC (this study) by the same enzymes. For pBAD33-yfp-popZΔN, *popZΔNstop* was amplified from a CB15N colony with primers CJW1740 + CJW1753, cut with KpnI and EcoRI, and ligated into pXYFPN-2 cut with the same enzymes. *yfp-popZΔN* was then amplified from the resulting plasmid with primers CJW1546 + CJW1753, digested with NdeI and HindIII, and ligated with pBAD33 cut out from pBAD33-popZ-TC (this study) by the same enzymes.

pNDM220-parA$_{R195E}$-cfp. *parA$_{R195E}$-cfp* was amplified from pACYC-ParA$_{R195E}$-ECFP (Schofield et al., 2010) using primers CJW1816 and CJW1037, digested with BamHI and XhoI, and ligated into the pNDM220 vector (low copy plasmid carrying the *lac* promoter and *lacIq*; gift from K. Gerdes, Center for Bacterial Cell Biology, Institute for Cell and Molecular Biosciences, Newcastle University, Newcastle, England, UK) cut with the same enzymes.

pVCFPC-4-parA$_{R195E}$. *parA$_{R195E}$* was amplified from pACYC-ParA$_{R195E}$-ECFP (Schofield et al., 2010) using primers CJW1186 and CJW1188, digested with KpnI and EcoRI, and ligated with pVCFPC-4 cut with the same enzymes.

pCFPC-4-popZ. *popZ* was amplified from CB15N using primers CJW1733 and CJW1734, digested with KpnI and EcoRI, and ligated with pCFPC-4 cut with the same enzymes.

Vectors for integration of tagged *dnaN* at the *dnaN* locus in *C. crescentus*. A 3′ fragment of *dnaN* was amplified from a CB15N colony using primers CJW1822 and CJW1823. The PCR product was digested with NdeI and KpnI and ligated into pCHYC-1 and pCFPC-1, both digested with the same enzymes, to construct pCHYC-1–dnaNend and pCFPC-1–dnaNend, respectively. Plasmids were integrated at the *dnaN* locus of CB15N genome, and the resultant strain was used as a donor for phage transduction to obtain strains harboring the *dnaN*::pCFPC-1–dnaN or *dnaN*::pCHYC-1–dnaN construct.

Vectors for integration of tagged *parA$_{K20R}$* at the *Pxyl* locus in *C. crescentus*. A joint PCR strategy was used to amplify *parA$_{K20R}$*. A first fragment was amplified from a CB15N colony using primers CJW1817 and CJW1818 (containing the K20R mutation). A second fragment was amplified from a CB15N colony using primers CJW1819 (complementary to CJW1818) and CJW1820. Both fragments were mixed and used as a template for joint PCR using primers CJW1817 and CJW1820. The resulting PCR product was blunt ligated into a pBluescript II (KS+) linearized with EcoRV, giving pBluescriptII(KS+)-parA$_{K20R}$. To construct pXCHYC-2–parA$_{K20R}$, *parA$_{K20R}$* was amplified from pBluescriptII(KS+)-parA$_{K20R}$ using primers CJW1821 and CJW1820, digested with NdeI and EcoRI, and ligated into pXCHYC-2 cut with the same enzymes. To construct pXTCYC-2-parA$_{K20R}$, *parA$_{K20R}$* was cut out of pXCHYC-2 with NdeI and EcoRI and ligated into pXTCYC-2 cut with the same enzymes.

pBAD18kan plasmids. *popZ-yfp* or *popZ-TC* were amplified from the pBAD33-popZ-yfp or pBAD33-popZ-TC plasmid using primers CJW1892 and CJW1897 or CJW1892 and CJW1895, respectively. The PCR products were digested with KpnI and XbaI and ligated into pBAD18kan (Guzman et al., 1995) digested with the same enzymes to obtain pBAD18kan-popZ-yfp and pBAD18kan-popZ-TC.

pMMB22-divIVA-parA$_{R195E}$-cfp. *parA$_{R195E}$-cfp* was amplified from the pNDM220-parA$_{R195E}$-cfp plasmid using primers CJW1867 and CJW1869, digested with XbaI and XhoI, and ligated into the pMMB22 vector cut out of pZD6 (gift from P. Christie, University of Texas-Houston Medical School, Houston, TX; Ding et al., 2002) with the same enzymes.

Multiple alignment

100 sequences of the 116 BLASTP (Protein Basic Local Alignment Search Tool) hits (highest e value of 2×10^{-8}) obtained using PopZ as a query were aligned by COBALT (NCBI). The alignment shown on Fig. 2 A was displayed with Jalview (Waterhouse et al., 2009) using the Clustal default color scheme (Larkin et al., 2007).

Native PAGE, SDS-PAGE, and Western blot

For the preparation of native samples, exponentially growing cells were harvested when OD_{660} was ≈0.2–0.3, after 3 h of induction of PopZ-YFP variants synthesis with xylose (0.03%). The pellet was resuspended in lysis buffer (50 mM Tris, 100 mM NaCl, and 0.5 mM EDTA, pH 7.5, at 4°C, freshly supplemented with 1 mM DTT, 1 mg/ml lysozyme, and one tablet of EDTA-free protease inhibitor cocktail [Complete; Roche] per 50 ml). This suspension was spun down for 10 min at 8,000 *g* at 4°C, and the pellet was resuspended in lysis buffer before sonication in a water–ice bath. Sonicated samples were spun down for 15 min at 8,000 *g* at 4°C, and the supernatant was diluted in 2× native PAGE loading buffer (0.16 M Tris-HCl, pH 6.8, 20% glycerol, 10% β-mercaptoethanol, and 0.4 mg/ml bromophenol blue) or 2× SDS-PAGE buffer (Laemmli, 1970) as indicated. All samples were kept on ice before loading on a 4–20% Mini-PROTEAN TGX Precast Gel (Bio-Rad Laboratories) for electrophoresis at 4°C in Tris-glycine native PAGE running buffer (3.03 g/liter Tris base and 14.4 g/liter glycine). For SDS-PAGE sample preparation, exponentially growing cells at OD_{660} of ≈0.2–0.3 were spun down, and the pellet was resuspended and boiled in 2× SDS-PAGE buffer. Resolved proteins were electrotransferred to polyvinylidene difluoride membranes, which were probed with an α-GFP antibody (1:2,000; Living Colors JL-8, #632381; BD). We used Precision Plus Protein All Blue Standards (Bio-Rad Laboratories) and NativeMark Unstained Protein Standard (Invitrogen) as molecular weight markers for SDS-PAGE and native PAGE, respectively. The polyvinylidene difluoride membrane was briefly stained with Ponceau (Sigma-Aldrich) after electrotransfer to visualize the NativeMark Unstained Protein Standards and to mark their approximate positions on the membrane for reference.

Microscopy image acquisition and analysis

For all microscopy observations, cells were spotted on 1% agarose pads (containing M2G- or M9-based medium for *C. crescentus* or *E. coli* strains,

respectively) between a glass slide and a coverslip. When applicable, cells were stained with 0.025 mg/ml DAPI and/or FlAsH (30-min incubation with 5 µM FlAsH and 20 µM 1,2-ethanedithiol in the appropriate culture medium at growth temperature). Live-cell imaging was performed using either an Eclipse 80i microscope (Nikon) equipped with a camera (Orca-II-ER; Hamamatsu Photonics; DIC objective Plan Apochromat VC 100×/1.40 NA [Nikon] or phase-contrast objective Plan Apochromat 100×/1.40 NA, optivar 1.5× [Nikon] when appropriate) or an Eclipse Ti-U microscope (Nikon) with a liquid crystal display camera (Orca-ER; Hamamatsu Photonics; phase-contrast objective Plan Apochromat 100×/1.40 NA [Nikon]) at room temperature except for time-lapse experiments (30°C). Images were acquired and processed with MetaMorph software (Molecular Devices), and cell meshes were obtained using the open source, MATLAB-based software MicrobeTracker (Sliusarenko et al., 2011). Spots were automatically detected on fluorescence images using the SpotFinderZ tool from MicrobeTracker, with parameters trained for each set of images, or manually recorded with SpotFinderM. Further quantitative analysis from cell meshes was performed with MATLAB (MathWorks, Inc.). Kymographs of fluorescence intensity (normalized by cell area and corrected for photobleaching) were obtained as described for the built-in kymograph function of MicrobeTracker. To obtain mean kymographs for a cell population, the fluorescence profiles obtained for each cell (as for single kymographs) were averaged for each time point. For Fig. 6 (C and E) and Fig. S4 H, we considered that MipZ-CFP or PopZ-YFP reached the new pole when the fluorescence intensity at the new pole (calculated as the new pole-proximal fifth portion of the cell) was at least equal to 20% of the total fluorescence intensity in the cell (based on empirical measurements). To determine cell polarity, cell meshes were oriented using the PopZ-YFP fluorescence signal profile at the first time point of the time lapse (when cells are in the swarmer stage); the half of the cell that contained the most PopZ-YFP intensity was defined as the old pole proximal.

Online supplemental material

Fig. S1 provides supporting data on the PopZ variants. Fig. S2 shows that the selective PopZ matrix can be detected by phase-contrast microscopy. Fig. S3 shows the cellular concentration and the diffusing fraction of PopZ during the cell cycle. Fig. S4 shows data supporting the experiments on novobiocin-treated, TipN-depleted, and A22-treated cells. Fig. S5 shows the expanded selective matrix formed by the ΔN PopZ variant as well as supporting data for the experiments on $ParA_{K20R}$-producing *C. crescentus* cells and on the DivIVA fusions in *E. coli*. Tables S1 and S2 list the strains and primers used in this study, respectively. Online supplemental material is available at http://www.jcb.org/cgi/content/full/jcb.201303036/DC1.

We thank Dr. Peter Christie for the kind gift of pZD6 and pZD22 plasmids, Dr. Gitte Ebersbach for initiating experiments with cephalexin, Hoong Chuin Lim for advices regarding the native PAGE experiments, Jorge Dinis and Lionel Schille for helping with the collection of novobiocin data, Dr. Oleksii Sliusarenko and Ahmad Paintdakhi for assistance with some of the MATLAB codes, and all the members of the Jacobs-Wagner laboratory for critical reading of this manuscript and for fruitful discussions.

G. Laloux was in part supported by the Belgian American Educational Foundation. This work was supported by the National Institutes of Health (R01 GM065835).

Submitted: 11 March 2013
Accepted: 30 April 2013

References

Bowman, G.R., L.R. Comolli, J. Zhu, M. Eckart, M. Koenig, K.H. Downing, W.E. Moerner, T. Earnest, and L. Shapiro. 2008. A polymeric protein anchors the chromosomal origin/ParB complex at a bacterial cell pole. *Cell*. 134:945–955. http://dx.doi.org/10.1016/j.cell.2008.07.015

Bowman, G.R., L.R. Comolli, G.M. Gaietta, M. Fero, S.-H. Hong, Y. Jones, J.H. Lee, K.H. Downing, M.H. Ellisman, H.H. McAdams, and L. Shapiro. 2010. *Caulobacter* PopZ forms a polar subdomain dictating sequential changes in pole composition and function. *Mol. Microbiol.* 76:173–189. http://dx.doi.org/10.1111/j.1365-2958.2010.07088.x

Bowman, G.R., A.I. Lyuksyutova, and L. Shapiro. 2011. Bacterial polarity. *Curr. Opin. Cell Biol.* 23:71–77. http://dx.doi.org/10.1016/j.ceb.2010.10.013

Cole, C., J.D. Barber, and G.J. Barton. 2008. The Jpred 3 secondary structure prediction server. *Nucleic Acids Res.* 36(Suppl. 2):W197-W201. http://dx.doi.org/10.1093/nar/gkn238

Collier, J., and L. Shapiro. 2009. Feedback control of DnaA-mediated replication initiation by replisome-associated HdaA protein in *Caulobacter*. *J. Bacteriol.* 191:5706–5716. http://dx.doi.org/10.1128/JB.00525-09

Curtis, P.D., and Y.V. Brun. 2010. Getting in the loop: regulation of development in *Caulobacter crescentus*. *Microbiol. Mol. Biol. Rev.* 74:13–41. http://dx.doi.org/10.1128/MMBR.00040-09

Ding, Z., Z. Zhao, S.J. Jakubowski, A. Krishnamohan, W. Margolin, and P.J. Christie. 2002. A novel cytology-based, two-hybrid screen for bacteria applied to protein-protein interaction studies of a type IV secretion system. *J. Bacteriol.* 184:5572–5582. http://dx.doi.org/10.1128/JB.184.20.5572-5582.2002

Ebersbach, G., A. Briegel, G.J. Jensen, and C. Jacobs-Wagner. 2008. A self-associating protein critical for chromosome attachment, division, and polar organization in *Caulobacter*. *Cell*. 134:956–968. http://dx.doi.org/10.1016/j.cell.2008.07.016

Edwards, D.H., H.B. Thomaides, and J. Errington. 2000. Promiscuous targeting of *Bacillus subtilis* cell division protein DivIVA to division sites in *Escherichia coli* and fission yeast. *EMBO J.* 19:2719–2727. http://dx.doi.org/10.1093/emboj/19.11.2719

Ely, B. 1991. Genetics of *Caulobacter crescentus*. *Methods Enzymol.* 204:372–384. http://dx.doi.org/10.1016/0076-6879(91)04019-K

Guzman, L.M., D. Belin, M.J. Carson, and J. Beckwith. 1995. Tight regulation, modulation, and high-level expression by vectors containing the arabinose PBAD promoter. *J. Bacteriol.* 177:4121–4130.

Jensen, R.B., S.C. Wang, and L. Shapiro. 2001. A moving DNA replication factory in *Caulobacter crescentus*. *EMBO J.* 20:4952–4963. http://dx.doi.org/10.1093/emboj/20.17.4952

Kiekebusch, D., K.A. Michie, L.-O. Essen, J. Löwe, and M. Thanbichler. 2012. Localized dimerization and nucleoid binding drive gradient formation by the bacterial cell division inhibitor MipZ. *Mol. Cell*. 46:245–259. http://dx.doi.org/10.1016/j.molcel.2012.03.004

Laemmli, U.K. 1970. Cleavage of structural proteins during the assembly of the head of bacteriophage T4. *Nature*. 227:680–685. http://dx.doi.org/10.1038/227680a0

Landgraf, D., B. Okumus, P. Chien, T.A. Baker, and J. Paulsson. 2012. Segregation of molecules at cell division reveals native protein localization. *Nat. Methods*. 9:480–482. http://dx.doi.org/10.1038/nmeth.1955

Larkin, M.A., G. Blackshields, N.P. Brown, R. Chenna, P.A. McGettigan, H. McWilliam, F. Valentin, I.M. Wallace, A. Wilm, R. Lopez, et al. 2007. Clustal W and Clustal X version 2.0. *Bioinformatics*. 23:2947–2948. http://dx.doi.org/10.1093/bioinformatics/btm404

Lenarcic, R., S. Halbedel, L. Visser, M. Shaw, L.J. Wu, J. Errington, D. Marenduzzo, and L.W. Hamoen. 2009. Localisation of DivIVA by targeting to negatively curved membranes. *EMBO J.* 28:2272–2282. http://dx.doi.org/10.1038/emboj.2009.129

Mohl, D.A., and J.W. Gober. 1997. Cell cycle-dependent polar localization of chromosome partitioning proteins in *Caulobacter crescentus*. *Cell*. 88:675–684.

Mohl, D.A., J.J. Easter Jr., and J.W. Gober. 2001. The chromosome partitioning protein, ParB, is required for cytokinesis in *Caulobacter crescentus*. *Mol. Microbiol.* 42:741–755. http://dx.doi.org/10.1046/j.1365-2958.2001.02643.x

Ptacin, J.L., S.F. Lee, E.C. Garner, E. Toro, M. Eckart, L.R. Comolli, W.E. Moerner, and L. Shapiro. 2010. A spindle-like apparatus guides bacterial chromosome segregation. *Nat. Cell Biol.* 12:791–798. http://dx.doi.org/10.1038/ncb2083

Ramamurthi, K.S., and R. Losick. 2009. Negative membrane curvature as a cue for subcellular localization of a bacterial protein. *Proc. Natl. Acad. Sci. USA*. 106:13541–13545. http://dx.doi.org/10.1073/pnas.0906851106

Ramamurthi, K.S., S. Lecuyer, H.A. Stone, and R. Losick. 2009. Geometric cue for protein localization in a bacterium. *Science*. 323:1354–1357. http://dx.doi.org/10.1126/science.1169218

Robinow, C., and E. Kellenberger. 1994. The bacterial nucleoid revisited. *Microbiol. Rev.* 58:211–232.

Rudner, D.Z., and R. Losick. 2010. Protein subcellular localization in bacteria. *Cold Spring Harb. Perspect. Biol.* 2:a000307. http://dx.doi.org/10.1101/cshperspect.a000307

Saberi, S., and E. Emberly. 2010. Chromosome driven spatial patterning of proteins in bacteria. *PLOS Comput. Biol.* 6:e1000986. http://dx.doi.org/10.1371/journal.pcbi.1000986

Schofield, W.B., H.C. Lim, and C. Jacobs-Wagner. 2010. Cell cycle coordination and regulation of bacterial chromosome segregation dynamics by polarly localized proteins. *EMBO J.* 29:3068–3081. http://dx.doi.org/10.1038/emboj.2010.207

Shebelut, C.W., J.M. Guberman, S. van Teeffelen, A.A. Yakhnina, and Z. Gitai. 2010. *Caulobacter* chromosome segregation is an ordered multistep process. *Proc. Natl. Acad. Sci. USA*. 107:14194–14198. http://dx.doi.org/10.1073/pnas.1005274107

Sliusarenko, O., J. Heinritz, T. Emonet, and C. Jacobs-Wagner. 2011. High-throughput, subpixel precision analysis of bacterial morphogenesis and intracellular spatio-temporal dynamics. *Mol. Microbiol.* 80:612–627. http://dx.doi.org/10.1111/j.1365-2958.2011.07579.x

Takacs, C.N., S. Poggio, G. Charbon, M. Pucheault, W. Vollmer, and C. Jacobs-Wagner. 2010. MreB drives de novo rod morphogenesis in *Caulobacter crescentus* via remodeling of the cell wall. *J. Bacteriol.* 192:1671–1684. http://dx.doi.org/10.1128/JB.01311-09

Thanbichler, M., and L. Shapiro. 2006. MipZ, a spatial regulator coordinating chromosome segregation with cell division in *Caulobacter. Cell*. 126:147–162. http://dx.doi.org/10.1016/j.cell.2006.05.038

Thanbichler, M., A.A. Iniesta, and L. Shapiro. 2007. A comprehensive set of plasmids for vanillate- and xylose-inducible gene expression in *Caulobacter crescentus*. *Nucleic Acids Res.* 35:e137. http://dx.doi.org/10.1093/nar/gkm818

Toro, E., S.-H. Hong, H.H. McAdams, and L. Shapiro. 2008. *Caulobacter* requires a dedicated mechanism to initiate chromosome segregation. *Proc. Natl. Acad. Sci. USA*. 105:15435–15440. http://dx.doi.org/10.1073/pnas.0807448105

Viollier, P.H., M. Thanbichler, P.T. McGrath, L. West, M. Meewan, H.H. McAdams, and L. Shapiro. 2004. Rapid and sequential movement of individual chromosomal loci to specific subcellular locations during bacterial DNA replication. *Proc. Natl. Acad. Sci. USA*. 101:9257–9262. http://dx.doi.org/10.1073/pnas.0402606101

Waterhouse, A.M., J.B. Procter, D.M.A. Martin, M. Clamp, and G.J. Barton. 2009. Jalview Version 2—a multiple sequence alignment editor and analysis workbench. *Bioinformatics*. 25:1189–1191. http://dx.doi.org/10.1093/bioinformatics/btp033

Winkler, J., A. Seybert, L. König, S. Pruggnaller, U. Haselmann, V. Sourjik, M. Weiss, A.S. Frangakis, A. Mogk, and B. Bukau. 2010. Quantitative and spatio-temporal features of protein aggregation in *Escherichia coli* and consequences on protein quality control and cellular ageing. *EMBO J.* 29:910–923. http://dx.doi.org/10.1038/emboj.2009.412